



ARTICLE


<https://doi.org/10.1038/s41467-022-29088-9>

OPEN

Microfluidic manipulation by spiral hollow-fibre actuators

Sitong Li¹, Rui Zhang ², Guanghao Zhang¹, Luyizheng Shuai¹, Wang Chang¹, Xiaoyu Hu¹, Min Zou¹, Xiang Zhou¹, Baigang An³, Dong Qian² & Zunfeng Liu ¹✉

A microfluidic manipulation system that can sense a liquid and control its flow is highly desirable. However, conventional sensors and motors have difficulty fitting the limited space in microfluidic devices; moreover, fast sensing and actuation are required because of the fast liquid flow in the hollow fibre. In this study, fast torsional and tensile actuators were developed using hollow fibres employing spiral nonlinear stress, which can sense the fluid temperature and sort the fluid into the desired vessels. The fluid-driven actuation exhibited a highly increased response speed (27 times as fast as that of air-driven actuation) and increased power density (90 times that of an air-driven solid fibre actuator). A 0.5 K fluid temperature fluctuation produced a 20° rotation of the hollow fibre. These high performances originated from increments in both heat transfer and the average bias angle, which was understood through theoretical analysis. This work provides a new design strategy for intelligent microfluidics and inspiration for soft robots and smart devices for biological, optical, or magnetic applications.

¹State Key Laboratory of Medicinal Chemical Biology, College of Chemistry and College of Pharmacy, Key Laboratory of Functional Polymer Materials, Frontiers Science Center for New Organic Matter, Nankai University, Tianjin 300071, China. ²Department of Mechanical Engineering, University of Texas at Dallas, Richardson, TX 75080, USA. ³School of Chemical Engineering, University of Science and Technology Liaoning, Anshan 114051, China.
✉email: liuzunfeng@nankai.edu.cn

Inspired by biofluidic systems, microfluidics have been developed and applied in various fields, such as in devices^{1,2}, biotechnology³⁻⁹, medicine^{10,11}, and electronics^{12,13}

normalise the rotation angle by the outer diameter. For a certain surface bias angle (α), the twist density (T) is inversely proportional to the fibre diameter (r) following the equation $\alpha = \tan^{-1}(2\pi rT)$ ⁶³. Therefore, a thinner fibre would rotate more than a thicker fibre for the same change in bias angle. Consequently, we multiplied the rotation angle by the outer diameter of the hollow-fibre actuator to obtain a normalised value. The $189^\circ \text{ cm}^{-1}$ rotation angle for the PEHF₅₈₀₋₉₉₀ actuator corre-

decreased from 0.5 to 0.25 g s⁻¹, and simultaneously, the response time of the actuator increased from 1.7 to 2.8 s (Supplementary Fig. 3a). As flowing 80 °C water in the homochiral PEHF actuator already resulted in coil-coil contact, the actuation stroke was maintained at a maximum value of 87.5% as the water flow rate decreased from 0.5 to 0.25 g s⁻¹ (Supplementary Fig. 3b).

As different sheath thicknesses of hollow fibres is generally used in microfluidics, in this section, we investigated the actuation performance as a function of the sheath thickness. Homochiral hollow-fibre actuators with different sheath thicknesses were prepared, which had the same surface bias angle (31.9°), pitch distance (9 mm), and spring index (4.0). Three types of PEHFs were used in this study: PEHF₃₈₀₋₁₀₉₀, PEHF₅₈₀₋₉₉₀, and PEHF₂₈₀₋₆₄₀, corresponding to sheath thicknesses of 710, 410, and 360 µm, respectively. Figure 3b and Supplementary Fig. 6a, b show images of these coiled hollow-fibre actuators during flowing of 95 °C water at a flow rate of 0.366 g s⁻¹ at different time. The decrease in the sheath thickness from 710 to 360 µm resulted in faster heat transfer, and the response time decreased from 3.2 to 1.0 s (Supplementary Fig. 6c). All the samples can form coil-coil contact, and there was a negligible difference in the actuation stroke for

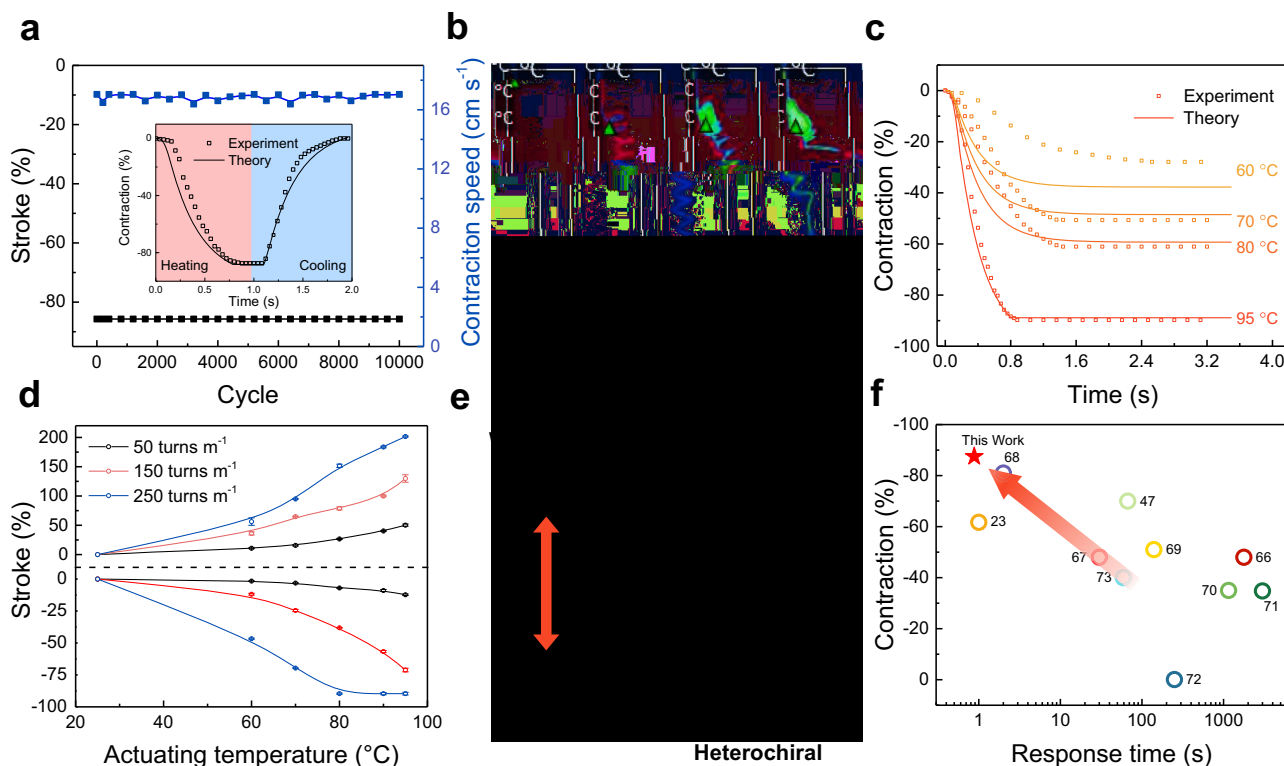


Fig. 3 Actuation performance of load-free tensile hollow-fibre actuators. **a** Tensile stroke and contraction speed during 10,000 fluid-driven heating-cooling actuation cycles. Inset: time dependence of contraction driven by alternatively flowing 90 °C and 25 °C water at a flow rate of 1.72 g s⁻¹. **b** Infrared images of the homochiral PEHF₅₈₀₋₉₉₀ actuators during water flow. **c** Experimental and theoretical results of a homochiral PEHF₅₈₀₋₉₉₀ actuator driven by flowing water at different temperatures. **d** Actuation stroke as a function of water temperature for heterochiral and homochiral PEHF₅₈₀₋₉₉₀ actuators with different inserted twist densities. **e** Schematic illustration and photograph of the heterochiral PEHF₅₈₀₋₉₉₀ actuator. **f** Comparison of the contraction and response time of PEHF₅₈₀₋₉₉₀ actuators with those of typical polymer fibre actuators reported in previous studies.

fibre, and the actuation stroke and actuation speed increased with increasing fluid temperature (Figs. 2e and 3c). These results show that the fluid-driven hollow-fibre actuator is hydrothermally driven, not hydraulically driven.

Next, we investigated the ability of the hollow-fibre actuator to carry a load (Fig. 4a), including the actuation stroke, actuation stress, specific work capacity, and cycling stability. For the convenience of expression, the isobaric stress was calculated as the weight of the load divided by the cross-sectional area of the sheath of the hollow fibre according to previously published papers^{49,58,63}. For better understanding, we also provide figures directly using the mass of the load in place of the stress in the supporting information (Fig. 4b, c and Supplementary Fig. 8).

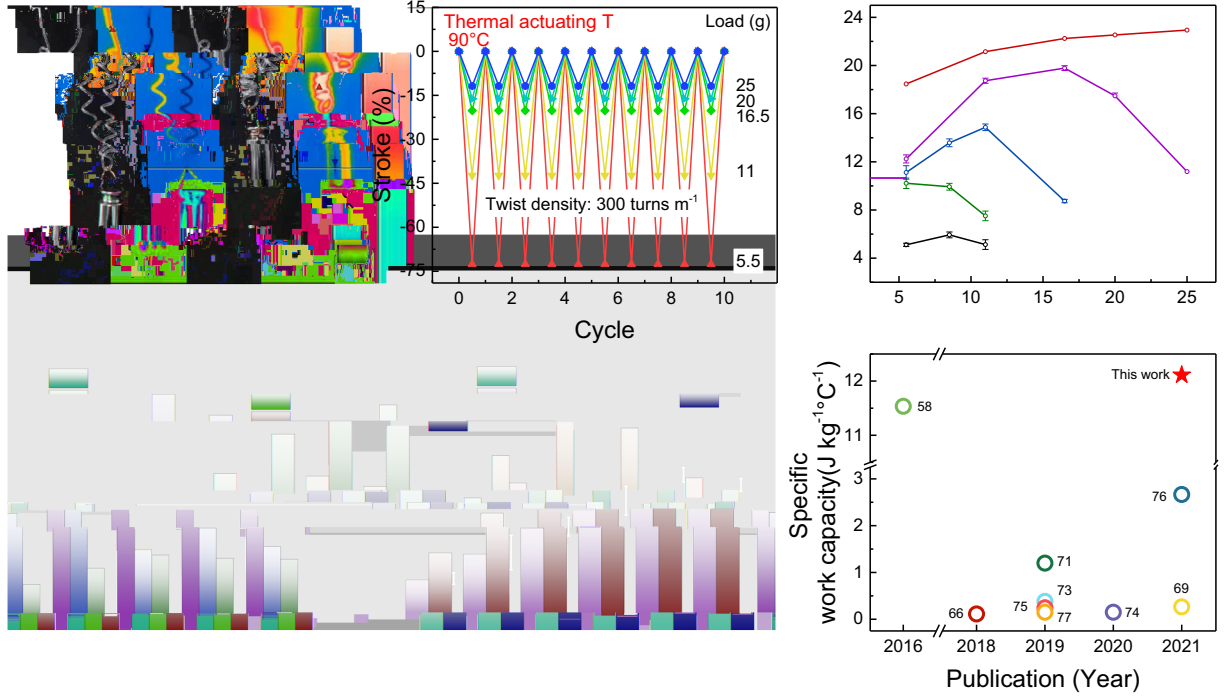
A homochiral PEHF₅₈₀₋₉₉₀ actuator, with a spring index of 4.0 and a pitch distance of 9 mm, was actuated by consecutively flowing water at 90 °C and 25 °C, achieving good repetitive actuation performance at different loading stresses (Fig. 4b and Supplementary Fig. 8a). By increasing the loading stress, the contractile stroke monotonically decreased, and the specific work output increased to a plateau of 0.25 MPa (Supplementary Fig. 8b). The specific work capacity increased with increasing twist density (Fig. 4c). As the bias angle at the outer surface is higher than that at the inner surface, we investigated whether hollow-fibre actuators with a higher sheath ratio realised higher work output, where the sheath ratio was defined as the sheath thickness divided by the outer diameter of the sheath. The work capacity increased with decreasing sheath ratio for a wide range of loading stresses (Fig. 4d). The power density of the PEHF₅₈₀₋₉₉₀ actuator was ~90 times (46.5 W kg⁻¹) that of an air-driven solid PE fibre (0.52 W kg⁻¹) (Supplementary Fig. 9), and the self-coiled

nylon 6 hollow-fibre actuator exhibited a specific work capacity (1.72 J g⁻¹) 1.5 times that of the solid nylon fibre actuator (1.13 J g⁻¹) with the same diameter (Fig. 4e). The combination of the actuation stroke (87.5%) and response time (0.88 s) is thus far the best among the polymer fibre actuators reported in previous studies^{23,47,66-73} (Fig. 3f), and the mass-normalised specific work capacity generated per Kelvin is also the best compared to the thermally driven individual polymer fibre actuators^{58,66,69,71,73-77} (Fig. 4f). Such high-performance parameters are a result of the combination of efficient heat transfer during fluid flow and the high average bias angle in the hollow fibre sheath.

Thermal-mechanical modelling of hollow-fibre actuators

As the hollow-fibre actuator was driven by flowing hot liquid, theoretically correlating the actuation behaviour with heat transfer is highly desirable to understand the actuation mechanism for design of hollow-fibre actuators for precise microfluidic manipulation. Therefore, we performed thermal-mechanical modelling of torsional and tensile hollow-fibre actuators by quantifying the heat transfer between the flowing liquid and hollow fibre (Supplementary Note 2). The temperature change of the hollow-fibre actuator is contributed by the forced convection of the flowing liquid (internal) and the natural convection of the ambient (external) air. To study this transient heat conduction problem, we established a two-step model. First, we modelled the radial heat conduction at an arbitrary cross-section of the hollow-fibre actuator by the following governing equations:

$$\frac{\partial^2 \theta}{\partial r^2} + \frac{1}{r} \frac{\partial \theta}{\partial r} = \frac{1}{\alpha} \frac{\partial \theta}{\partial t} \text{ in } R_i \leq r \leq R_o, \quad (1a)$$



$$k \frac{\partial \theta}{\partial r} = h_w (\theta - \theta_w) \text{ at } r = R_i, \quad (1b)$$

$$-k \frac{\partial \theta}{\partial r} = h_a (\theta - \theta_a) \text{ at } r = R_o, \quad (1c)$$

$$\theta = \theta_0 \text{ at } t = 0, \quad (1d)$$

where temperature θ is a function of the radial position r and time t , and the inner and outer radii of the hollow fibre are denoted by R_i and R_o , respectively. Thermal diffusivity $\alpha = k/\rho C_p$ is a material constant that depends on thermal conductivity k , mass density ρ , and specific heat capacity C_p . The convective heat transfer coefficients of water and air are represented by h_w and h_a , respectively. Similarly, θ_w and θ_a are the temperatures of water and air, respectively. Finally, θ_0 denotes the initial temperature of the fibre. Radial temperature $\theta(r, t)$ is obtained by solving the above set of one-dimensional partial differential equations (see Supplementary Note 2 for more details).

Thereafter, we constructed a simple axial temperature model dominated by convection due to water transport since the flow rate of the water is much higher than the axial heat conduction rate of the fibre. The basis for this assumption is as follows. First, the high aspect ratio of the hollow fibre makes the heating/cooling process much faster in the radial direction than in the axial direction of the hollow-fibre actuator when considering only heat conduction. Second, polymers are poor heat conductors. When analysing the heat transfer mechanisms in the axial direction of the actuator, convection due to the fast water transport plays a major role compared to the slow heat conduction inside the fibre,

which is evident from Supplementary Fig. 3a: the actuation response rate is very sensitive to the water flow rate.

Water temperature $\theta_w(x, t)$ depends on a few factors, for instance, the initial water temperature, water flow rate, and heat loss due to transfer to the hollow-fibre actuator and eventually to the ambient air. Since the heat loss is relatively low when the flow rate is high, we can simply approximate the water temperature as

$$\theta_w(x, t) = \theta_{w0} H(vt - x), \quad (2)$$

where θ_{w0} denotes the initial water temperature, v is the water flow rate, and $H(\cdot)$ is the Heaviside step function. By combining Eqs. (1) and (2), we determined the temperature of the hollow-fibre actuator as a function of the axial and radial positions and time, i.e., $\theta = \theta(x, r, t)$.

The torsional actuation mechanism of twisted polymer fibres has also been studied³⁹. Upon heating, the polymer chains expand in the radial direction and contract in the axial direction, which can be accommodated by changes in the length, diameter, and twist of the hollow fibre. The change in length is considered to be small, and the following equation for untwisting can be obtained⁵⁸:

$$\Delta T = \left(\frac{\Delta \lambda}{\lambda} \frac{1}{\cos^2 \alpha_f} - \frac{\Delta d}{d} \right) T, \quad (3)$$

where T denotes the twist density, ΔT denotes the untwist during torsional rotation, d and Δd are the diameter of the hollow fibre and its change, respectively, and λ and $\Delta \lambda$ are the length and length change of the helically oriented polymer chain, respectively. Furthermore, this equation can be rewritten as

follows:

$$\Delta T = \left(\alpha_{\lambda} \frac{1}{\cos^2 \alpha_f} - \alpha_d \right) \Delta \theta \cdot T \quad (4)$$

where $\alpha_{\lambda} = -(5.3 \pm 0.4) \times 10^{-4} \text{K}^{-1}$ and $\alpha_d = (5.2 \pm 0.7) \times 10^{-4} \text{K}^{-1}$ are the respective axial and radial thermal expansion coefficients of PEHFs obtained from thermomechanical analysis (TMA). In this work, the average exterior hollow-fibre temperature change $\Delta \theta = \theta_w(x, t)$ is employed as the actuation temperature.

The tensile actuation mechanism of a coiled polymer fibre is well documented in Ref. ⁵⁸, and is described as follows:

$$\frac{\Delta L}{L} = \frac{l^2}{NL} \Delta T \quad (5)$$

where L and ΔL denote the coil length and change in the coil length, respectively; l is the length of the twisted hollow fibre; and N is the number of coil turns.

Using these equations, the torsional and tensile actuation of hollow-fibre actuators were theoretically obtained. The temperature as a function of radial and axial positions and time can be solved using Eqs. (1) and (2). Then, the torsional actuation is obtained from Eq. (4). Finally, the tensile actuation is given by Eq. (5). The temperature solutions to Eqs. (1) and (2) are numerically solved in this work.

These theoretical results are consistent with the experimental results (Figs. 2c, f, 3a, c, and Supplementary Fig. 6c). The percent length change ($\Delta L/L$) of the tensile actuator is linearly related to the twist change (ΔT) of the twisted hollow fibre (Eq. 5), which is monotonically correlated with the temperature change ($\Delta \theta$) of the hollow-fibre actuator (Eq. 4). Forced convection of axial water flow contributes to the actuator temperature, which monotonically correlates with the initial water temperature and water flow rate (Eq. 2). Therefore, we observe that the actuation stroke and response time are monotonically correlated with the water temperature and water flow rate (Figs. 2e, 3c, d and Supplementary Figs. 3b and 7a).

The response time can be related to the water temperature by examining the transient heat conduction equation (Eq. 1a in this context). A higher water temperature will provide a sharper temperature gradient. According to Eq. (1a), this will lead to a higher rate of change for the temperature.

Hollow-fibre actuators for microfluidic sensing and manipulation

In high-throughput biosensing or medicine synthesis, a liquid containing specific chemicals is transported to certain vessels for chemical reactions^{78,79}. Because temperature is an important factor influencing reactions, ensuring that the liquid with the required temperature flows into the desired vessel is important for precise control of chemical reactions^{80,81}. However, during microfluid transport, the temperature may vary over time. Therefore, sensing the liquid temperature and sorting the liquid into the desired vessels are highly desirable for microfluidic manipulation. In the conventional design, the sorting devices contain different modules, such as sensors (for temperature measurement) and motors (for moving the tubes for transporting liquid) (Supplementary Fig. 10a), which require complex design and lead to a bulky size.

In this work, torsional and tensile hollow-fibre actuators were employed for microfluidic manipulation, which can precisely rotate and translate the transported liquid according to the liquid temperature (Supplementary Movies 2 to 4). The torsional hollow-fibre actuator can rotate to different angles when flowing liquid at different temperatures (Fig. 5a). Here, a 20-cm-long

torsional PEHF₅₈₀₋₉₉₀ actuator with an inserted twist density of 400 turns m^{-1} was provided for torsional microfluidic manipulation. A 96-well plate was placed below the PEHF₅₈₀₋₉₉₀ actuator to collect the liquid, which was transported at a flow rate of 100 mg s^{-1} . For a 0.5 K fluid temperature change (e.g., from 30 to 30.5 °C), the actuator rotated by 20° (Fig. 5b). The temperature resolution and normalised torsional rotation per Kelvin of this actuator are better than those of other thermally driven twisted actuators in previous studies^{39,63,82-87} (Fig. 5c). Further changes in temperature resulted in a linear increase in the rotation angle with fluid temperature (Fig. 5d). Consequently, fluids with different temperatures can be sorted into the desired wells. Similarly, the homochiral hollow-fibre actuator can contract to different lengths when transporting liquids at different temperatures (Fig. 1b and Supplementary Fig. 10b), and a contractile actuator can transport and sort a liquid at different temperatures by contracting to different lengths (Supplementary Figs. 10c, d and Supplementary Movie 4).

We also demonstrated employment of the hollow-fibre actuator as a clamp to capture an object. A homochiral PEHF₅₈₀₋₉₉₀ actuator was wrapped around a mandrel and thermally annealed at 108 °C for 1 h to set the shape, and it was used as a soft clamp to capture a 2-g load. By flowing 80 °C water at a flow rate of 1.72 g s^{-1} , the actuator shrank and tightly trapped the load during continuous water flow, which was then lifted by hand. Stopping the supply of the water flow resulted in a temperature decrease of the actuator and release of the load (Supplementary Movie 5). This provides the possibility for hollow-fibre actuators to be employed in soft robotics and industrial manufacturing as artificial muscles with fast response speed and large stroke.

Discussions

Compared to actuators driven by electroheating or air heating, fluid-flow-driven hollow-fibre actuators require setups for pumping, heating, and storing the liquid. These requirements can limit the application, and addressing these requirements would facilitate application of hollow-fibre actuators in a wide range of scenarios and provide additional opportunities for the design of fluid-driven smart materials and devices.

We investigated the dependence of the stability of the fluid-driven hollow-fibre actuators on the environmental conditions (temperature, moisture, and wind) and type of fluid (Supplementary Fig. 2). The results indicate that the relative change in rotation angle is less than 5% for the investigated experimental conditions, indicating that stable actuation performance was obtained. This agrees with the theoretical understanding, in which the heat transfer coefficient for air convection is 1-2 orders of magnitude smaller than that for convective heat transfer of liquid. Therefore, such liquid-flow-driven actuation of a hollow-fibre actuator showed good tolerance against environmental changes. To decrease the disturbance of actuation caused by environmental fluctuations, use of a high flow speed, a high actuation temperature, or a large-size hollow-fibre actuator is suggested. We also examined the actuation dependence on the type of applied fluid, fluid viscosity, and fluid density, and there is a negligible change in the actuation performance when actuated by the different investigated types of fluid (Supplementary Figs. 2d and 4). Decreasing the cooling temperature resulted in decreased hysteresis during heating/cooling cycles (Supplementary Fig. 5).

We summarise the response time of the hollow-fibre actuators investigated in this work in two tables. The response time is in the range of 0.88 to 3 s (Supplementary Tables 1 and 2), which are among the best values reported for thermally driven actuators

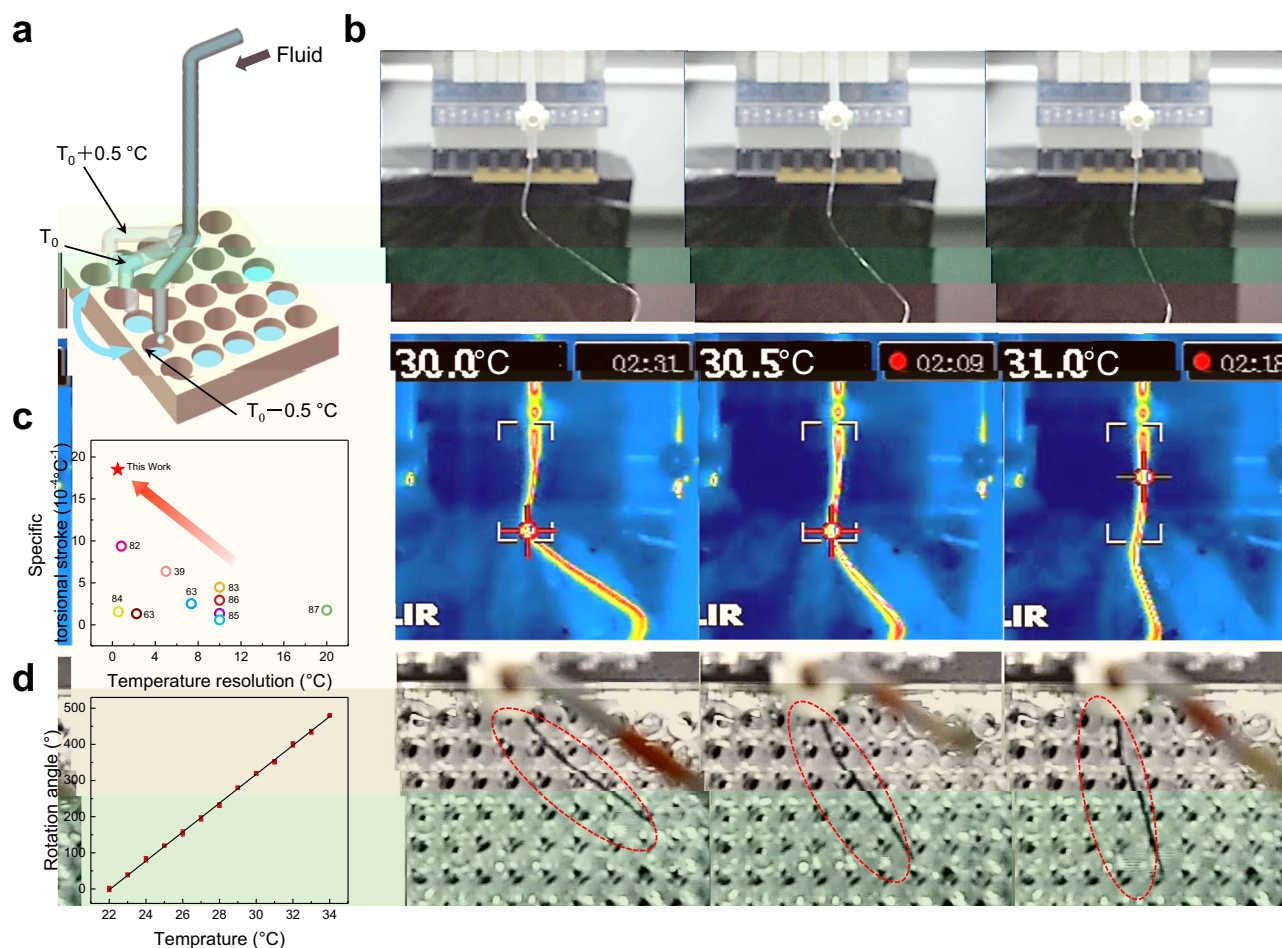


Fig. 5 Microfluidic sensing and manipulation by PEHF₅₈₀₋₉₉₀ actuators. **a** Schematic of the microfluidic sensing and manipulation device. **b** Optical images of PEHF₅₈₀₋₉₉₀ actuators for sensing the liquid temperature and sorting the liquid into the desired vessels. **c** Comparison of the temperature resolution and specific torsional stroke of PEHF₅₈₀₋₉₉₀ with those in previous studies. The specific torsional stroke is defined as $\Delta T / (T \cdot \Delta \theta)$, where ΔT denotes the thermally driven torsional rotation, T denotes the twist density, and $\Delta \theta$ is the temperature change. The temperature resolution is the minimum temperature change used to trigger torsional actuation. **d** Torsional angle as a function of water temperature.

(Fig. 3f). The response time can be decreased by enhancing the forced convection between the fluid and hollow fibre and the heat transfer in the hollow fibre. These enhancements can be realised by increasing the fluid flow rate and fluid temperature, decreasing the wall thickness, and decreasing the fibre length of the hollow-fibre actuator.

From Eq. (5), we conclude that the resolution of the tensile actuation of the coiled hollow-fibre actuator ($\Delta L/L$) is proportional to $l^2 \Delta T / NL$, and from Eq. (4), we can obtain ΔT ; therefore, the $\Delta L/L$ for a temperature change of 1 K can be obtained from Eqs. (4) and (5) (where l is the fibre length, L and ΔL are the coil length and its change, respectively, ΔT is the change in twist density, and N is the coil number). Supplementary Table 3 shows the relevant parameters of the homochiral hollow-fibre muscles and the resolution for a temperature change of 1 K. The length change of the muscles is up to $\sim 3\%$ in this work.

We tried to obtain the optimised geometry of the hollow fibre (Supplementary Note 3). From the equation (Supplementary Eq. 3.4), the material should be distributed as far as possible from the centre of the cross-section, which justifies the use of hollow fibre over solid cross-sections. Note that the above theoretically derived optimum geometry is subject to the constraint that the hollow fibre will not buckle under the applied torque. Thus, in

practice, a hollow fibre with finite thickness should be used for the proposed actuation application.

In conclusion, a compact microfluidic manipulation system that can sense the liquid temperature and sort the liquid was developed by employing spiral hollow-fibre actuators. The fast sensing and manipulation originated from the indispensable combination of stress generation in the spiral hollow fibre sheath and efficient heat transfer during liquid flow. Additionally, this strategy is readily applicable to existing microfluidic tubing materials. In response to fluid flow, the resulting actuator could function with a high actuation stroke (87.5%), a fast response speed (0.88 s), and high temperature sensitivity (20° rotation for a temperature change of 0.5 K). The work capacity and power density were 1.5 times and 90 times those of air-driven solid fibres, respectively. This microfluidic manipulation design could be a new platform for high-throughput biosensing and medicine synthesis. The fast response and high power density of the fluid-driven actuator ensure its application in exoskeletons and artificial muscles, for instance, for developing powerful soft robots and automatic production lines. Moreover, the unique design provides new opportunities for developing equipment for biomarker sensing and drug control release, 3D printers, morphing aircraft, intelligent buildings, and other optical or magnetic applications.

Methods

Materials and methods

Preparation of the hollow fibre actuators. PEHF₂₈₀₋₆₄₀, PEHF₅₈₀₋₉₉₀, and PEHF₃₈₀₋₁₀₉₀ and solid PE fibre (with a diameter of 1 mm) were obtained from Yongfa Plastic Products Co. Ltd). Nylon 6 hollow fibre (with inner and outer diameters of 0.1 mm and 0.4 mm) and nylon 6 fibre (with a diameter of 0.4 mm) are purchased from Sensa Fishing Import and Export Co., Ltd. All the hollow fibres were used as received.

Different types of fluids were employed to drive the actuation of the hollow fibre actuator, including ethanol (EtOH), iso-propanol (IPA), glycerol, acetone, dimethyl sulfoxide (DMSO), N, N-dimethylformamide (DMF), dichloromethane (DCM), tetrahydrofuran (THF), toluene, ethyl acetate (EA), and petroleum ether (PE), which were obtained from Shanghai Aladdin Biochemical Technology Co., Ltd. NaCl (Shanghai Macklin Biochemical Co., Ltd) was employed to prepare the fluid with different densities.

Before twist insertion, the hollow fibre was inserted with a copper wire (the diameter was slightly smaller than that of the inner diameter of the hollow fibre). The top end of the copper-wire-containing hollow fibre was connected to a 42-step servomotor (Huatian Technology Co., Ltd.), and its bottom end was isobarically loaded with 0.53 MPa weight. The load was torsionally tethered during twist insertion to avoid twist release⁵⁰. During twist insertion, the bottom end of the PEHF was tethered and twist was inserted from the top side. The bottom end of the copper wire was not tethered and allowed to rotate during twist insertion, which enabled it to be easily removed after sample preparation. After twist insertion, the copper-wire-containing PEHF was both ends tethered and thermally annealed in an oven at a 108 °C for 1 h to thermally set the shape. The torsional hollow fibre actuator was obtained after cooling to room temperature and removing the copper wire. The coiled PEHF actuator was prepared by wrapping the twisted, copper-wire-containing hollow fibre on a mandrel, followed by annealing at 108 °C for 1 h. The solid PE fibre and the nylon 6 hollow fibre were twisted in the same way, and the tensile coiled nylon 6 actuators were prepared by twisting the nylon 6 fibre until self-coiling under a 23.4 MPa stress and annealing at 180 °C for 2 h.

Actuation of the hollow fibre actuators. Water-driven actuation was carried out by pumping water into the twisted or coiled hollow fibres using a water pump (Mini K-DCS10, Kamoer Fluid Tech Co., Ltd.) Actuation driven by hot air was carried out in a temperature-controlled oven. A thermal camera (FLIR T440) was used to monitor the surface temperature of the hollow fibre during actuation. The surface of the hollow fibre showed uniform temperature during actuation by water flow.

In this study different parameters were studied. While if not specified, the water temperature was 95 °C, and the water flow rate was 0.5 g s⁻¹; the torsional hollow fibre actuator was a PEHF₅₈₀₋₉₉₀ actuator with twist density of 400 turns mm⁻¹; the homochiral hollow fibre actuator was a PEHF₅₈₀₋₉₉₀ actuator with spring index of 4.0, coil pitch of 9 mm, and the twist density was 200 turns m⁻¹; the heterochiral hollow fibre actuator was a PEHF₅₈₀₋₉₉₀ actuator with spring index of 4.0, no coil pitch, and the twist density was 200 turns m⁻¹. The hollow-fibre actuators were trained for 3 cycles to obtain repetitive actuation performances.

Data availability

The authors declare that all data supporting the findings of this study are available within the main text and Supplementary Information. Source data are provided with this paper.

Received: 31 August 2021; Accepted: 16 February 2022;

Published online: 14 March 2022

References

- Stroock A. D. Chapter 17 - MICROFLUIDICS. In: *Optical Biosensors (Second Edition)* (eds Ligler F. S., Taitt C. R.). (Elsevier, 2008).
- Stelson, A. C. et al. Label-free detection of conformational changes in switchable DNA nanostructures with microwave microfluidics. *Nat. Commun.* **10**, 1174 (2019).
- Shin, S. R. et al. Aptamer-based microfluidic electrochemical biosensor for monitoring cell-secreted trace cardiac biomarkers. *Anal. Chem.* **88**, 10019–10027 (2016).
- Burns, M. A. et al. An integrated nanoliter dna analysis device. *Science* **282**, 484–487 (1998).
- Yager, P. et al. Microfluidic diagnostic technologies for global public health. *Nature* **442**, 412–418 (2006).
- Maxwell, E. J., Mazzeo, A. D. & Whitesides, G. M. Paper-based electroanalytical devices for accessible diagnostic testing. *MRS Bull.* **38**, 309–314 (2013).
- Lombardo, J. A., Aliaghaei, M., Nguyen, Q. H., Kessenbrock, K. & Haun, J. B. Microfluidic platform accelerates tissue processing into single cells for molecular analysis and primary culture models. *Nat. Commun.* **12**, 2858 (2021).
- Nightingale, A. M. et al. Monitoring biomolecule concentrations in tissue using a wearable droplet microfluidic-based sensor. *Nat. Commun.* **10**, 2741 (2019).
- Srivastava, N. & Burns, M. A. Analysis of non-newtonian liquids using a microfluidic capillary viscometer. *Anal. Chem.* **78**, 1690–1696 (2006).
- Eduati, F. et al. A microfluidics platform for combinatorial drug screening on cancer biopsies. *Nat. Commun.* **9**, 2434 (2018).
- Schuster, B. et al. Automated microfluidic platform for dynamic and combinatorial drug screening of tumor organoids. *Nat. Commun.* **11**, 5271 (2020).
- van Erp, R., Soleimanzadeh, R., Nela, L., Kampitsis, G. & Mantioli, E. Co-designing electronics with microfluidics for more sustainable cooling. *Nature* **585**, 211–216 (2020).
- Guo, J. et al. Microfluidics for flexible electronics. *Mater. Today* **44**, 105–135 (2021).
- Whitesides, G. M. The origins and the future of microfluidics. *Nature* **442**, 368–373 (2006).
- Google Patents. <https://patents.google.com/patent/US8431387B2/en>.
- Google Patents. <https://patents.google.com/patent/US7544506B2/en>.
- Xu, L., Lee, H., Jetta, D. & Oh, K. W. Vacuum-driven power-free microfluidics utilizing the gas solubility or permeability of polydimethylsiloxane (PDMS). *Lab Chip* **15**, 3962–3979 (2015).
- Jang, I. & Song, S. Facile and precise flow control for a paper-based microfluidic device through varying paper permeability. *Lab Chip* **15**, 3405–3412 (2015).
- Barbot, A., Wales, D., Yeatman, E. & Yang, G. Z. Microfluidics at fiber tip for nanoliter delivery and sampling. *Adv. Sci.* **8**, 2004643 (2021).
- Wang, Z. et al. Self-powered viscosity and pressure sensing in microfluidic systems based on the piezoelectric energy harvesting of flowing droplets. *ACS Appl. Mater. Interfaces* **9**, 28586–28595 (2017).
- Lin, H. et al. A programmable epidermal microfluidic valving system for wearable biofluid management and contextual biomarker analysis. *Nat. Commun.* **11**, 4405 (2020).
- Dunne, P. et al. Liquid flow and control without solid walls. *Nature* **581**, 58–62 (2020).
- Yu, N. et al. Thermal-responsive anisotropic wetting microstructures for manipulation of fluids in microfluidics. *Langmuir* **33**, 494–502 (2017).
- ter Schiphorst, J. et al. Molecular design of light-responsive hydrogels, for in situ generation of fast and reversible valves for microfluidic applications. *Chem. Mater.* **27**, 5925–5931 (2015).
- Satarkar, N. S., Zhang, W., Eitel, R. E. & Hilt, J. Z. Magnetic hydrogel nanocomposites as remote controlled microfluidic valves. *Lab Chip* **9**, 1773–1779 (2009).
- Li, L. et al. In-channel responsive surface wettability for reversible and multifunctional emulsion droplet preparation and applications. *ACS Appl. Mater. Interfaces* **11**, 16934–16943 (2019).
- Zhao, S. et al. Bio-functionalized silk hydrogel microfluidic systems. *Biomaterials* **93**, 60–70 (2016).
- Lin, H. et al. Fabrication of asymmetric tubular hydrogels through polymerization-assisted welding for thermal flow actuated artificial muscles. *Chem. Mater.* **31**, 4469–4478 (2019).
- Lv, J. A. et al. Photocontrol of fluid slugs in liquid crystal polymer microactuators. *Nature* **537**, 179–184 (2016).
- Xu, B., Zhu, C., Qin, L., Wei, J. & Yu, Y. Light-directed liquid manipulation in flexible bilayer microtubes. *Small* **15**, e1901847 (2019).
- Liu, Q., Liu, Y., Lv, J. A., Chen, E. & Yu, Y. Photocontrolled liquid transportation in microtubes by manipulating mesogen orientations in liquid crystal polymers. *Adv. Intell. Syst.* **1**, 1900060 (2019).
- Srinivasan, V., Pamula, V. K. & Fair, R. B. An integrated digital microfluidic lab-on-a-chip for clinical diagnostics on human physiological fluids. *Lab Chip* **4**, 310–315 (2004).
- Link, D. R. et al. Electric control of droplets in microfluidic devices. *Angew. Chem. Int. Ed. Engl.* **45**, 2556–2560 (2006).
- Wang, T. et al. Janus Si micropillar arrays with thermal-responsive anisotropic wettability for manipulation of microfluid motions. *ACS Appl. Mater. Interfaces* **7**, 376–382 (2015).
- Benito-Lopez, F., Antonana-Diez, M., Curto, V. F., Diamond, D. & Castro-Lopez, V. Modular microfluidic valve structures based on reversible thermoresponsive ionogel actuators. *Lab Chip* **14**, 3530–3538 (2014).
- Beebe, D. J. et al. Functional hydrogel structures for autonomous flow control inside microfluidic channels. *Nature* **404**, 588–590 (2000).
- Liu, G. L., Kim, J., Lu, Y. & Lee, L. P. Optofluidic control using photothermal nanoparticles. *Nat. Mater.* **5**, 27–32 (2006).
- Baigl, D. Photo-actuation of liquids for light-driven microfluidics: state of the art and perspectives. *Lab Chip* **12**, 3637–3653 (2012).
- Li, J. et al. Photothermal bimorph actuators with in built cooler for light mills, frequency switches, and soft robots. *Adv. Funct. Mater.* **29**, 1808995 (2019).

40. Aziz, S., Naficy, S., Foroughi, J., Brown, H. R. & Spinks, G. M. Controlled and scalable torsional actuation of twisted nylon 6 fiber. *J. Polym. Sci., Part B: Polym. Phys.* **54**, 1278–1286 (2016).
41. Mirvakili, S. M. & Hunter, I. W. Fast torsional artificial muscles from niti twisted yarns. *ACS Appl. Mater. Interfaces* **9**, 16321–16326 (2017).
42. Li, Y. et al. Moisture-sensitive torsional cotton artificial muscle and textile. *Chin. Phys. B* **29**, 048103 (2020).
43. Son, W. et al. Highly twisted supercoils for superelastic multi-functional fibres. *Nat. Commun.* **10**, 426 (2019).
44. Guo, W. et al. A novel electromechanical actuation mechanism of a carbon nanotube fiber. *Adv. Mater.* **24**, 5379–5384 (2012).
45. Zou, M. et al. Progresses in tensile, torsional, and multifunctional soft actuators. *Adv. Funct. Mater.* **31**, 2007437 (2021).
46. Mirvakili, S. M. & Hunter, I. W. Artificial muscles: mechanisms, applications, and challenges. *Adv. Mater.* **30**, 1704407 (2018).
47. Jia, T. et al. Moisture sensitive smart yarns and textiles from self-balanced silk fiber muscles. *Adv. Funct. Mater.* **29**, 1808241 (2019).
48. Mu, J. et al. Sheath-run artificial muscles. *Science* **365**, 150–155 (2019).
49. Kanik, M. et al. Strain-programmable fiber-based artificial muscle. *Science* **365**, 145–150 (2019).
50. Wang, R. et al. Tensile and torsional elastomer fiber artificial muscle by entropic elasticity with thermo-piezoresistive sensing of strain and rotation by a single electric signal. *Mater. Horiz.* **7**, 3305–3315 (2020).
51. Chen, P. et al. Hierarchically arranged helical fibre actuators driven by solvents and vapours. *Nat. Nanotechnol.* **10**, 1077–1083 (2015).
52. Deng, J. et al. Preparation of biomimetic hierarchically helical fiber actuators from carbon nanotubes. *Nat. Protoc.* **12**, 1349–1358 (2017).
53. Chen, J. et al. High-performance natural melanin/poly(vinyl alcohol-co-ethylene) nanofibers/ pa6 fiber for twisted and coiled fiber-based actuator. *Adv. Fiber Mater.* **2**, 64–73 (2020).
54. Kim, H. et al. Biomimetic color changing anisotropic soft actuators with integrated metal nanowire percolation network transparent heaters for soft robotics. *Adv. Funct. Mater.* **28**, 1801847 (2018).
55. Yin, Z. et al. Sweat-driven silk-yarn switches enabled by highly aligned gaps for air-conditioning textiles. *Adv. Fiber Mater.* **1**, 197–204 (2019).
56. Yuan, J. et al. Shape memory nanocomposite fibers for untethered high-energy microengines. *Science* **365**, 155–158 (2019).
57. Wang, Y. et al. High-twist-permeated electrochemical yarn muscles with ultralarge and fast contractile actuations. *Mater. Horiz.* **7**, 3043–3050 (2020).
58. Haines, C. S. et al. Artificial muscles from fishing line and sewing thread. *Science* **343**, 868–872 (2014).
59. Baughman, R. H. Negative thermal expansion in crystalline linear polymers. *J. Chem. Phys.* **58**, 2976–2983 (1973).
60. Kobayashi, Y. & Keller, A. The temperature coefficient of the c lattice parameter of polyethylene; an example of thermal shrinkage along the chain direction. *Polymer* **11**, 114–117 (1970).
61. Choy, C., Chen, F. & Young, K. Negative thermal expansion in oriented crystalline polymers. *J. Polym. Sci. Polym. Phys. Ed.* **19**, 335–352 (1981).
62. Aziz, S. & Spinks, G. M. Torsional artificial muscles. *Mater. Horiz.* **7**, 667–693 (2020).
63. Lima, M. D. et al. Electrically, chemically, and photonically powered torsional and tensile actuation of hybrid carbon nanotube yarn muscles. *Science* **338**, 928–932 (2012).
64. Cheng, H. et al. Moisture-activated torsional graphene-fiber motor. *Adv. Mater.* **26**, 2909–2913 (2014).
65. Hu, X., Leng, X., Jia, T. & Liu, Z. Twisted and coiled bamboo artificial muscles for moisture responsive torsional and tensile actuation. *Chin. Phys. B* **29**, 118103 (2020).
66. Chin, S. M. et al. Covalent-supramolecular hybrid polymers as muscle-inspired anisotropic actuators. *Nat. Commun.* **9**, 2395 (2018).
67. Sarikaya, S. et al. Athermal artificial muscles with drastically improved work capacity from pH-Responsive coiled polymer fibers. *Sens. Actuators B Chem.* **335**, 129703 (2021).
68. Leng, X. et al. Tuning the reversibility of hair artificial muscles by disulfide cross-linking for sensors, switches, and soft robotics. *Mater. Horiz.* **8**, 1538–1546 (2021).
69. Kotikian, A. et al. Innervated, self-sensing liquid crystal elastomer actuators with closed loop control. *Adv. Mater.* **33**, e2101814 (2021).
70. Qian, X. et al. Untethered recyclable tubular actuators with versatile locomotion for soft continuum robots. *Adv. Mater.* **30**, 1801103 (2018).
71. Yang, Y. et al. Reprocessable thermoset soft actuators. *Angew. Chem. Int. Ed. Engl.* **58**, 17474–17479 (2019).
72. Maziz, A. et al. Knitting and weaving artificial muscles. *Sci. Adv.* **3**, e1600327 (2017).
73. He, Q. et al. Electrically controlled liquid crystal elastomer-based soft tubular actuator with multimodal actuation. *Sci. Adv.* **5**, eaax5746 (2019).
74. Jiang, Z. C., Xiao, Y. Y., Yin, L., Han, L. & Zhao, Y. "Self-lockable" liquid crystalline diels-alder dynamic network actuators with room temperature programmability and solution reprocessability. *Angew. Chem. Int. Ed. Engl.* **59**, 4925–4931 (2020).
75. Liu, J. et al. Shaping and locomotion of soft robots using filament actuators made from liquid crystal elastomer-carbon nanotube composites. *Adv. Intell. Syst.* **2**, 1900163 (2020).
76. Aziz, S. et al. A microwave powered polymeric artificial muscle. *Appl. Mater. Today* **23**, 101021 (2021).
77. Gao, P., Li, J. & Shi, Q. A hollow polyethylene fiber-based artificial muscle. *Adv. Fiber Mater.* **1**, 214–221 (2019).
78. Du, G., Fang, Q. & den Toonder, J. M. Microfluidics for cell-based high throughput screening platforms - a review. *Anal. Chim. Acta* **903**, 36–50 (2016).
79. Wang, Z., Kim, M. C., Marquez, M. & Thorsen, T. High-density microfluidic arrays for cell cytotoxicity analysis. *Lab Chip* **7**, 740–745 (2007).
80. Hung, L. H. & Lee, A. P. Microfluidic devices for the synthesis of nanoparticles and biomaterials. *J. Med. Biol. Eng.* **27**, 1–6 (2007).
81. Brivio, M., Verboom, W. & Reinhoudt, D. N. Miniaturized continuous flow reaction vessels: influence on chemical reactions. *Lab Chip* **6**, 329–344 (2006).
82. Suh, D., Truong, T. K., Suh, D. G. & Lim, S. C. Torsional actuator powered by environmental energy harvesting from diurnal temperature variation. *ACS Sustain. Chem. Eng.* **4**, 6647–6652 (2016).
83. Kim, H. et al. Thermally responsive torsional and tensile fiber actuator based on graphene oxide. *ACS Appl. Mater. Interfaces* **10**, 32760–32764 (2018).
84. Farhan, M., Rudolph, T., Kratz, K. & Lendlein, A. Torsional fiber actuators from shape-memory polymer. *MRS Adv.* **3**, 3861–3868 (2018).
85. Aziz, S., Naficy, S., Foroughi, J., Brown, H. R. & Spinks, G. M. Effect of anisotropic thermal expansion on the torsional actuation of twist oriented polymer fibres. *Polymer* **129**, 127–134 (2017).
86. Aziz, S., Naficy, S., Foroughi, J., Brown, H. R. & Spinks, G. M. Thermomechanical effects in the torsional actuation of twisted nylon 6 fiber. *J. Appl. Polym. Sci.* **134**, 45529 (2017).
87. Kongahage, D., Spinks, G. M. & Foroughi, J. Twisted and coiled multi-ply yarns artificial muscles. *Sens. Actuators, A* **318**, 112490 (2021).

Acknowledgements

This work was supported by the National Key Research and Development Program of China (grants 2019YFE0119600), the National Natural Science Foundation of China (grants 51973093, 51773094, and U1533122), Frontiers Science Center for New Organic Matter, Nankai University (Grant Number 63181206), the National Special Support Plan for High-Level Talents People, the Science Foundation for Distinguished Young Scholars of Tianjin (grant no. 18JCJCQ46600), the Xingliao Talent Plan (XLYC1802042), the Fundamental Research Funds for the Central Universities (grant 63171219), the State Key Laboratory for Modification of Chemical Fibers and Polymer Materials, Donghua University (grant LK1704), the grant from the US National Science Foundation (Award CMMI-1727960), and Eugene McDermott Graduate Fellowship at The University of Texas at Dallas.

Author contributions

Z.F.L. and S.L. were responsible for the experimental concept and design. S.L., G.Z., L.S., W.C., X.Z., X.H., B.A. and M.Z. carried out the most experiments, characterisation and data analyses. R.Z. and D.Q. contributed to theoretical simulation and calculation. Z.F.L. was responsible for project administration, conceptualisation, supervision, formal analysis, funding acquisition, validation, writing original draft, review and editing. All authors wrote the paper. All authors provided comments and agreed with the final form of the manuscript.

Competing interests

The authors declare no competing interests.

Additional information

Supplementary information The online version contains supplementary material available at <https://doi.org/10.1038/s41467-022-29088-9>.

Correspondence and requests for materials should be addressed to Zunfeng Liu.

Peer review information *Nature Communications* thanks Shazed Aziz, Xiaoming Tao and the other, anonymous, reviewer(s) for their contribution to the peer review of this work. Peer reviewer reports are available.

Reprints and permission information is available at <http://www.nature.com/reprints>

Publisher's note Springer Nature remains neutral with regard to jurisdictional claims in published maps and institutional affiliations.



Open Access This article is licensed under a Creative Commons Attribution 4.0 International License, which permits use, sharing, adaptation, distribution and reproduction in any medium or format, as long as you give appropriate credit to the original author(s) and the source, provide a link to the Creative Commons license, and indicate if changes were made. The images or other third party material in this article are included in the article's Creative Commons license, unless indicated otherwise in a credit line to the material. If material is not included in the article's Creative Commons license and your intended use is not permitted by statutory regulation or exceeds the permitted use, you will need to obtain permission directly from the copyright holder. To view a copy of this license, visit <http://creativecommons.org/licenses/by/4.0/>.

© The Author(s) 2022